JOURNAL OF SYNCHROTRON RADIATION

ISSN 1600-5775

Compact undulator line for a high-brilliance soft-X-ray free-electron laser at MAX IV

Alan Mak, Peter Salén and Vitaliy Goryashko*

FREIA Laboratory, Uppsala University, PO Box 516, SE-751 20 Uppsala, Sweden.
*Correspondence e-mail: vitaliy.goryashko@physics.uu.se

Received 16 November 2018
Accepted 25 February 2019

Edited by I. Lindau, SLAC/Stanford University, USA

Keywords: undulator technologies; X-ray free-electron lasers; high brilliance; self-amplified spontaneous emission; harmonic lasing self-seeding.

The optimal parameter space for an X-ray free-electron laser (FEL) in the self-amplified spontaneous emission (SASE) operation mode is examined. This study focuses on FEL operation with a shorter undulator period and higher undulator strength made available through recent developments in in-vacuum, cryogenic and superconducting undulators. Progress on short-period undulator technologies is surveyed and FEL output characteristics *versus* undulator parameters are computed. The study is performed on a case of the planned soft-X-ray FEL at the MAX IV Laboratory in Sweden. An extension of the SASE mode into the harmonic lasing self-seeded mode is also analysed.

1. Introduction

The X-ray free-electron laser (FEL) is a coherent and tunable light source offering a spatial resolution at the ångström scale and a temporal resolution at the femtosecond and subfemtosecond scales. It delivers the highest peak brilliance amongst laboratory X-ray sources today, outperforming even the synchrotron by five to ten orders of magnitude (see Fig. 1).

Thanks to these superb optical properties, the X-ray FEL has opened up many new frontiers in solid-state physics (Bencivenga *et al.*, 2015), photochemistry (Ullrich *et al.*, 2012), structural biology (Neutze *et al.*, 2015) and other research disciplines. In the soft X-ray spectral region, the FEL has proven useful for coherent diffraction imaging and time-resolved X-ray spectroscopy. The former is performed routinely at the FLASH (Chapman *et al.*, 2006; Mancuso *et al.*, 2010) and FERMI (Capotondi *et al.*, 2013, 2015) facilities. The latter has been applied to the studies of, for instance, artificial photosynthesis (Smolentsev & Sundström, 2015) and correlations between valence electrons and holes (Mukamel *et al.*, 2013). The increasing number of scientific applications and the growing demand for beam time motivate the development of new FEL facilities.

However, the X-ray FEL facilities in operation today are generally very long; therefore, an ongoing quest in FEL research and development is to make the FEL more compact while seeking a higher brilliance (Huang, 2015). This is also the primary objective of the international project 'Compact Light' (Compact Light Collaboration, 2018–2020) funded by the European Union's Horizon 2020 Research and Innovation Programme.

One approach to a more compact FEL is to take advantage of the advancements (Huang *et al.*, 2017; Bahrdt & Gluskin, 2018) in cryogenic, superconducting and in-vacuum undulator technologies, so as to reduce the undulator length required for reaching a high brilliance. In this article, we study this approach by means of analytical calculations and numerical

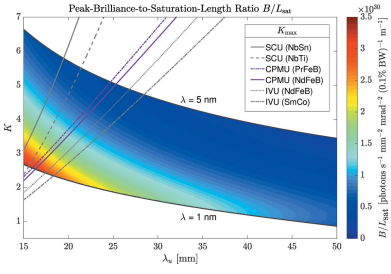

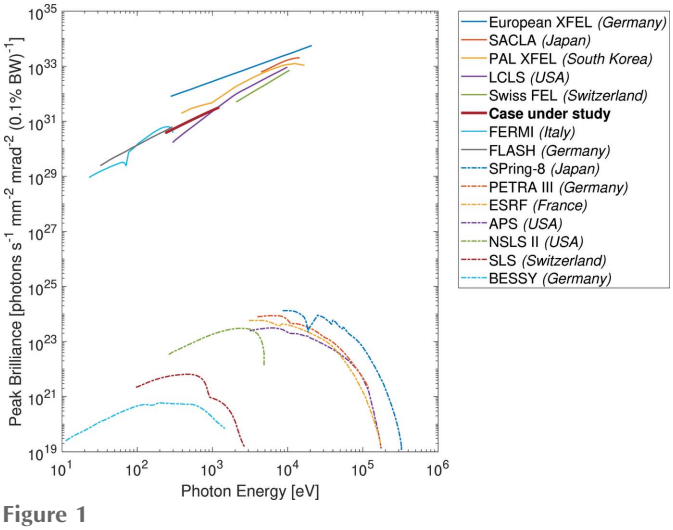

Figure 1
Peak brilliance as a function of photon energy for a selected set of light sources. FEL facilities and synchrotron facilities are shown in solid and dashed lines, respectively. This figure is adapted from Figure 1 in the work by Weckert (2015). The curve labelled 'case under study' is produced from analytical calculations using the electron parameters in Table 2 and an undulator period of 20 mm.

simulations, on a case involving the Soft X-ray Laser (SXL) project (Werin *et al.*, 2017) at the MAX IV Laboratory in Sweden.

Though some scientific applications of the FEL such as magnetization dynamics (Seddon *et al.*, 2017) and chirality of molecules (Cahn *et al.*, 1966) require polarization control, most applications can benefit from the preferential direction of a linearly polarized field. Hence, even next-generation FEL facilities such as LCLS-II (Galayda, 2018) and the European XFEL (Altarelli, 2007) are primarily based on planar undulators.

In this study, we focus on the planar undulator configuration, which produces linearly polarized FEL radiation. Elliptically polarized (or polarization-tunable) radiation can be produced by deploying a main planar undulator line that is reversely tapered, followed by an afterburner. The former serves to suppress the radiation at the fundamental harmonic, while allowing the formation of microbunches as in the standard FEL operation (Schneidmiller & Yurkov, 2013). The latter is a helical undulator segment, in which the microbunched electron beam can radiate coherently and produce ellipically polarized FEL fields. Using this approach, the degree of desired circular polarization experimentally demonstrated at LCLS was around 98% (Lutman *et al.*, 2016).

In contrast to a planar undulator, a helical undulator has a magnetic field which couples more efficiently to the electron beam motion, and has an undulator parameter that is $\sqrt{2}$ times that of a planar undulator with the same period. With a higher undulator parameter, the helical configuration can lead to a more compact undulator line.

However, this advantage is outweighed by the mechanical complexity in the tuning of the undulator parameter. To tune the FEL wavelength, the undulator magnetic field must be adjustable, and this is more easily achievable with the planar configuration. For instance, for a planar undulator, the magnetic field strength can be adjusted by displacing one row of magnets with respect to the other along the length of the undulator. In contrast, a helical undulator usually requires four rows of magnets to be movable in the radial direction, which is technically more challenging. Despite years of development, 'tunable' cryogenic permanent magnet helical undulators are still in the R&D phase and have not been demonstrated yet (Bahrdt *et al.*, 2018).

Another advantage of the tunable planar undulator line over the helical one is the enhanced longitudinal coherence for a certain wavelength range. To this end, the undulator line is effectively split into two sections such that the desired output wavelength is set as the fundamental wavelength in the second section but is set as a higher harmonic in the first section. As the fundamental wavelength in the first section is longer, the cooperation time (and hence, the longitudinal coherence) can be increased. This mode of operation is known as harmonic lasing self-seeding (HLSS) (Schneidmiller & Yurkov, 2012). In this paper, we focus on the baseline design of a planar undulator line for the SXL project. We also investigate the HLSS mode.

2. Theoretical background

2.1. General remarks

The FEL has two main components: a beam of relativistic electrons and an undulator. In the undulator, the electron beam interacts with and amplifies the radiation that it emits. In this article, we consider the operation mode of self-amplified spontaneous emission (SASE) (Kondratenko & Saldin, 1980; Bonifacio *et al.*, 1984), whereby the growth in radiation power starts from the shot noise in the electron beam.

The undulator is a magnetic device with a temporally static and spatially periodic magnetic field along its length. The magnetic field is specified by two parameters: the undulator period λ_u and the undulator parameter,

$$K = \frac{e\lambda_u B_0}{2\pi m_e c}, \tag{1}$$

where B_0 is the magnetic field amplitude, e is the absolute value of the electron charge, m_e is the electron rest mass and c is the speed of light.

On the axis of the undulator, the fundamental wavelength of the radiation is given by

$$\lambda = \frac{\lambda_u}{2\gamma^2}\left(1 + a_u^2\right), \tag{2}$$

where $a_u = K/\sqrt{2}$ for a planar undulator and $a_u = K$ for a helical undulator. The Lorentz factor γ denotes the electron energy in units of the rest energy $m_e c^2$.

A figure of merit for a FEL is the peak brilliance (see Fig. 1), which is the number of photons emitted per unit time, per unit cross-sectional area, per unit solid angle within a bandwidth (BW) of 0.1% of the central wavelength. A related quantity is

the average brilliance, which is the peak brilliance multiplied by the duration of the light pulse and the repetition rate.

The peak brilliance and other FEL properties can be calculated analytically from the 1D and 3D theories, which are recapitulated in the appendices.

2.2. Magnetic field strength deliverable by an undulator

For the purpose of developing a compact FEL, it is advantageous to minimize the saturation length and maximize the peak brilliance. In turn, these require optimizing the undulator specifications, namely λ_u and K. According to equation (1), K is scaled linearly with the magnetic field strength B_0. In general, B_0 can be expressed by the Halbach formula (Halbach, 1983),

$$B_0(g, \lambda_u) = h_1 \exp\left[-h_2\left(\frac{g}{\lambda_u}\right) + h_3\left(\frac{g}{\lambda_u}\right)^2\right]. \quad (3)$$

Here g is the gap height, *i.e.* the separation between the two opposite rows of magnetic poles in the undulator. B_0 has the unit of tesla, while both λ_u and g have the unit of millimetre. The coefficients h_1, h_2 and h_3 have different values for different undulators types and for different materials. Table 1 shows four examples for the in-vacuum undulator (IVU) and the cryogenic permanent-magnet undulator (CPMU).

For the superconducting undulator (SCU), the scaling law for B_0 is different from equation (3). An alternative formulation was devised by Kim (2005) and summarized by Moog *et al.* (2017) as follows:

$$B_0(g, \lambda_u) = \left(0.28052 + 0.05798\lambda_u - 9\times10^{-4}\lambda_u^2 + 5\times10^{-6}\lambda_u^3\right) \times \exp\left[-\pi\left(\frac{g}{\lambda_u} - 0.5\right)\right]. \quad (4)$$

Here B_0 has the unit of tesla, while λ_u and g have the unit of millimetre. Note that equation (4) applies to NbTi superconducting wires at 80% of the critical current density. For Nb_3Sn superconducting wires, the expression is otherwise identical to equation (4), except that it needs to be multiplied by a factor of 1.3 (Moog *et al.*, 2017).

In both equation (3) and equation (4), B_0 can be increased by increasing λ_u or decreasing g. For any given λ_u, the largest achievable B_0 is limited by the smallest acceptable g, which is determined by the beam stay-clear. It then follows from equation (1) that

$$K_{max}(\lambda_u) = \frac{e}{2\pi m_e c}\lambda_u B_0(g_{min}, \lambda_u). \quad (5)$$

Using equation (5), we can calculate the maximum K deliverable as a function of λ_u for different undulator types and for different materials.

3. Results and discussions

3.1. Analytical calculations

Using the 3D FEL theory outlined in Appendix *B*, we perform analytical calculations for the Soft X-ray Laser (SXL) project (Werin *et al.*, 2017) at the MAX IV Laboratory in Sweden.

Table 1
Halbach coefficients for different undulator types.

Type	Material	h_1	h_2	h_3	Source
IVU	SmCo	2.94	4.62	1.37	Dejus *et al.* (2009)
IVU	NdFeB	3.28	4.51	1.20	Dejus *et al.* (2009)
CPMU	NdFeB	3.341	3.606	0.300	Dejus *et al.* (2009)
CPMU	PrFeB	3.502	3.604	0.359	Dejus *et al.* (2009)

Table 2
Electron parameters in the case under study.

Parameter	Symbol	Value
Electron energy	$\gamma m_e c^2$	3 GeV
Relative energy spread	σ_γ/γ	10^{-4}
Peak current	I_0	1.4 kA
Normalized emittance	ϵ_n	0.4 mm mrad
Average of beta function	$\bar{\beta}$	5 m

The SXL is a planned FEL facility that would utilize the electron beam from the existing linear accelerator at MAX IV. The target range for the radiation wavelength λ is 1–5 nm. Here we consider a case which uses (i) the SASE operation mode, (ii) variable-gap planar undulators and (iii) the electron parameter values shown in Table 2.

To investigate the dependence of the FEL performance on the undulator specifications, we examine the four colour maps in Fig. 2. Each colour map shows the variation of a performance parameter over the K–λ_u plane, specifically in the region corresponding to the target wavelength range of λ = 1–5 nm.

Given the undulator period λ_u, the desired wavelength λ can be obtained by adjusting the gap height g (and hence the undulator parameter K) to satisfy equation (2). Within Fig. 2(*a*), a larger λ_u yields a higher saturation power P_{sat}. Within Fig. 2(*b*), a smaller λ_u yields a smaller saturation length L_{sat}. Within Fig. 2(*c*), a smaller λ_u yields a longer coherence time τ_c. Within Fig. 2(*d*), a smaller λ_u yields a higher peak brilliance B.

For the purpose of developing a compact FEL, we want the largest B over the smallest L_{sat}. To this end, a useful figure of merit is the ratio B/L_{sat}, for which a colour map is shown in Fig. 3. Within the domain of Fig. 3, the largest B/L_{sat} occurs at λ_u = 15 mm.

However, not all regions of the K–λ_u plane are accessible in practice. For any given λ_u, there is an upper limit for K given by $K_{max}(\lambda_u)$ in equation (5). The grey and purple curves in Fig. 3 show the function $K_{max}(\lambda_u)$ for six combinations of undulator types and materials. The stay-clear gap is assumed to be 3.0 mm for all six scenarios. This corresponds to a magnetic gap of g = 4.8 mm for the undulator type of SCU, and g = 3.2 mm for the other undulator types.

One of the main constraints on g is the requirement that a relative energy spread induced in the beam by the resistive wakefield in an undulator vacuum chamber is less than the Pierce parameter ρ. For g = 3 mm, the induced relative energy

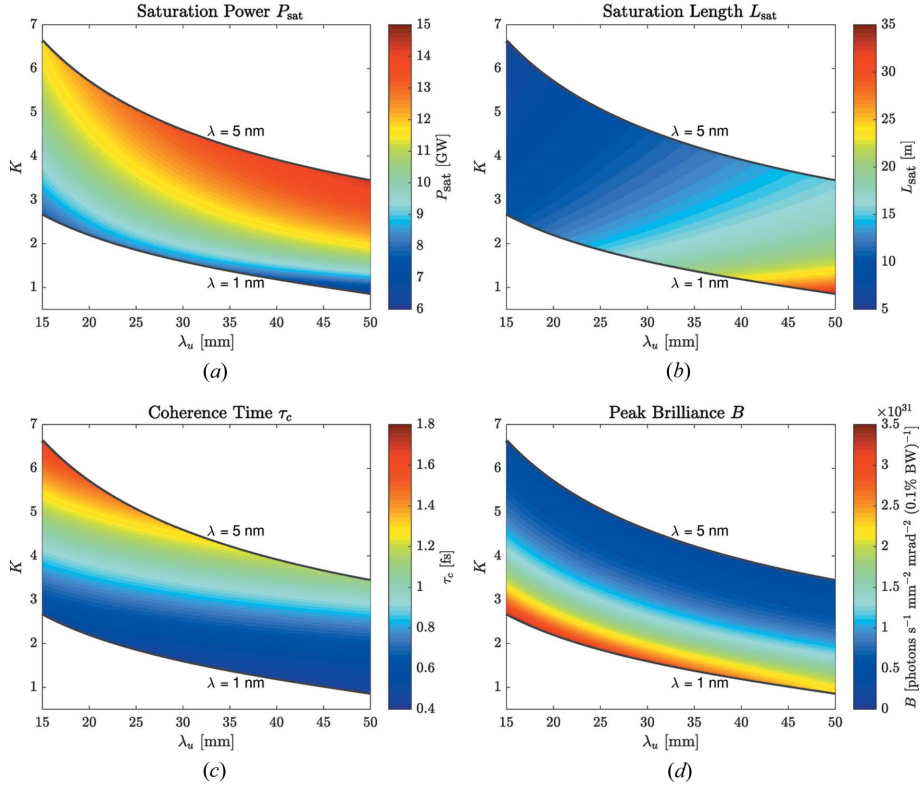

Figure 2
Colour maps showing the variations of the following four parameters over the K–λ_u plane, in the region corresponding to the wavelength range of λ = 1–5 nm: (*a*) saturation power P_{sat}, (*b*) saturation length L_{sat}, (*c*) coherence time τ_c at saturation and (*d*) peak brilliance B at saturation.

spread is estimated to be 0.2×10^{-3} according to the model by Craievich (2010). As λ_u ranges from 15 mm to 50 mm, ρ varies from 0.5×10^{-3} to 1.5×10^{-3}.

In each of the six scenarios, the accessible region of the K–λ_u plane is that below (and to the right of) the curve. Amongst the six scenarios, the undulator type of SCU with the Nb_3Sn material has the largest K_{max} at any given λ_u (see Fig. 3). However, in order to cover the entire target wavelength range of λ = 1–5 nm, the smallest possible choice for λ_u is 20 mm.

With λ_u = 20 mm, the peak brilliance B ranges from 3.9×10^{30} to 3.1×10^{31} photons s^{-1} mm^{-2} mrad^{-2} (0.1% bandwidth)$^{-1}$ in Fig. 2(*d*). This result is also shown in Fig. 1 by the curve labelled 'Case under study' to facilitate a comparison with existing FEL facilities.

In Fig. 1, the SASE FELs reaching the photon energy range of the case under study are: FLASH, LCLS, PAL XFEL and European XFEL. Note that FERMI is seeded and is not an SASE FEL. In terms of peak brilliance, the case under study is comparable with all the aforementioned SASE FELs, except the state-of-the-art European XFEL.

In terms of the undulator length, however, the case under study outperforms the existing FEL facilities significantly. In Fig. 2(*b*), with λ_u = 20 mm, the saturation length L_{sat} ranges from 7.7 to 12 m. This means that the total undulator length can be as short as 12 m in our case. Putting this into perspective, the total undulator length is 27 m for FLASH (Honkavaara, 2018) and 35 m for the soft-X-ray undulator line of the PAL XFEL (Ko *et al.*, 2017).

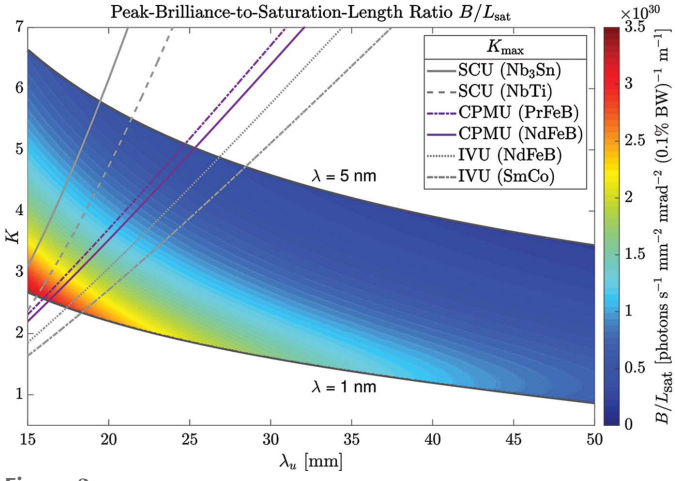

Figure 3
Colour map showing the variation of the ratio B/L_{sat} over the K–λ_u plane in the region corresponding to the wavelength range λ = 1–5 nm. Here B is the peak brilliance at saturation and L_{sat} is the saturation length. The grey and purple curves show the maximum K deliverable as a function of λ_u for different undulator types and for different materials.

3.2. Numerical simulations

We supplement the analytical calculations with numerical simulations, using the 3D and time-dependent simulation code GENESIS (Reiche, 1999).

In the simulations, the electron parameters remain the same as in Table 2. Meanwhile, we choose the operation point λ_u = 15 mm, K = 2.68 and λ = 1 nm, which corresponds to the largest B/L_{sat} in Fig. 3. This operation point is accessible by the SCU-type undulator with the Nb_3Sn material.

The undulator line of a SASE FEL is usually segmented, with individual undulator modules separated by break sections. The purpose of the break sections is to provide space for the installation of focusing magnets, corrector magnets, phase shifters, diagnostics instruments *etc.* In the simulations, each undulator module has a length of 2.7 m and each break section has a length of 0.6 m. This is summarized in Table 3.

The focusing lattice is in a FODO configuration. The strengths of the quadrupole magnets are adjusted to deliver the average beta value specified in Table 2.

The SASE operation mode has a stochastic nature. We therefore simulate a total of 99 SASE shots and examine the

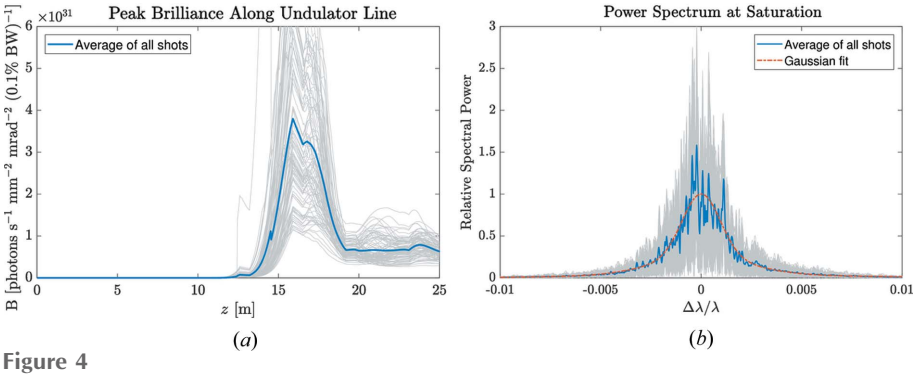

(*a*) (*b*)

Figure 4
Simulation results: (*a*) peak brilliance B as a function of the distance z along the undulator line; (*b*) power spectrum at the saturation point z = 15.9 m, with the vertical axis showing the spectral power relative to the peak value of the Gaussian fit. Each grey curve corresponds to one SASE shot, and the blue curve shows the average of all 99 shots.

Table 3
Operation point used in the numerical simulations.

Parameter	Symbol	Value
Radiation wavelength	λ	1 nm
Undulator period	λ_u	15 mm
Undulator parameter	K	2.68
Length of each undulator module	–	2.7 m
Length of each break section	–	0.6 m
RMS length of electron bunch	σ_z	9 µm

average behaviour. The results are shown in Fig. 4. Fig. 4(*a*) shows the evolution of the peak brilliance along the undulator line. If we define the saturation point as the point of maximum peak brilliance, then saturation occurs at z = 15.9 m with a peak brilliance of 3.7×10^{31} photons s^{-1} mm^{-2} mrad^{-2} (0.1% bandwidth)$^{-1}$. The discrepancy between the analytical and numerical results for the peak brilliance appears to be around 10%. Excluding the break sections, the net undulator length required to reach the saturation point is 13.5 m. Fig. 4(*b*) shows the power spectrum at the saturation point z = 15.9 m. Upon fitting the averaged spectrum to a Gaussian distribution, the r.m.s. bandwidth is found to be $\sigma_\lambda/\lambda = 1.1 \times 10^{-3}$.

3.3. Harmonic lasing self-seeding

A simple and robust upgrade option to the SASE configuration is provided by HLSS (Schneidmiller *et al.*, 2017), which offers an improved peak brilliance and a shorter saturation length without any need for additional hardware components. In this scheme, the undulator line is divided into two sections of different K values, such that the hth harmonic ($h > 1$) of the radiation produced in the first section serves as the seed at the fundamental wavelength for the second section. The harmonic lasing of the first section stays below saturation and the amplification proceeds to saturation in the second section. This enables the FEL system to benefit from both (i) the reduced bandwidth of the harmonic compared with the fundamental at the same wavelength and (ii) the higher saturation power of the fundamental. Consequently, an increased peak brilliance is obtained for which the enhancement factor over the corresponding SASE case is (Schneidmiller *et al.*, 2017)

$$R = \frac{h\left(L_u L_{\mathrm{sat},h}\right)^{1/2}}{L_{\mathrm{sat},1}}. \qquad (6)$$

Here L_u is the length of the first undulator section; $L_{\mathrm{sat},1}$ and $L_{\mathrm{sat},h}$ are the saturation lengths of the fundamental and the harmonic, respectively. See further details in Appendix *C*.

Fig. 5 shows the enhancement factor R, using $h = 3$, in the K–λ_u plane for the output wavelengths of λ = 1–1.67 nm. This wavelength interval can be accessed using the K-value range producing λ = 1–5 nm radiation in SASE mode. Here, we have assumed $L_u = 0.6 L_{\mathrm{sat},h}$, which is sufficiently short to stay well below saturation of the fundamental in the first section (Schneidmiller & Yurkov, 2012), but long enough to provide a significant enhancement of R. Fig. 5 also shows the required K values for the fundamental (blue lines) and the harmonic (black lines) as well as the maximum K-value for the SCU (Nb_3Sn) undulators. The enhancement of the peak brilliance compared with SASE using λ_u = 20 mm is R = 1.66–1.70 at the output wavelength range λ = 1–1.67 nm. Hence, a significant upgrade is achievable at the shortest wavelengths compared with the SASE case under study just by tuning the first undulator section to a higher K-value.

4. Conclusions

In this article, we have surveyed the recent progress on undulator technologies and studied analytically as well as

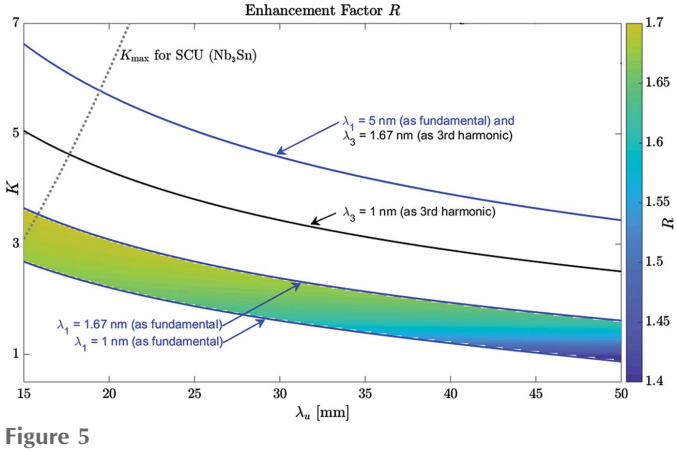

Figure 5
Colour map for the enhancement factor R for the peak brilliance upon switching from SASE to HLSS. In this example of HLSS, the third harmonic of the radiation produced in the first undulator section is equal to the fundamental wavelength for the second undulator section. For the K range corresponding to the wavelength range from 1 nm to 5 nm in the SASE mode, HLSS is operational from 1 nm to 1.67 nm. It can enhance the peak brilliance up to 1.7 times.

numerically a case involving a compact high-brilliance X-ray FEL.

For three undulator technologies – (i) in-vacuum, (ii) cryogenic and (iii) superconducting undulators – the analytical expressions for the peak magnetic field as a function of the undulator period and gap are presented. The Halbach coefficients for different undulator types and different magnetic materials are summarized in Table 1. We deduce the possible FEL performance for a stay-clear undulator gap of 3 mm such that the resistive wakefield introduces an energy spread compatible with FEL operation. For peak undulator fields in the tesla range, the minimum undulator period is in the range of 15–20 mm depending on the undulator technology (see Fig. 3).

The maps of parameter space for the optimal FEL operation are calculated analytically and a numerical example using the GENESIS simulation code is presented for a selected set of parameters. The results strongly indicate that state-of-the-art magnet-based undulator technologies would allow the shortening of the total required undulator length by more than a factor of two while preserving (or even improving) the X-ray brilliance.

Furthermore, keeping the SASE setup, the coherence and brilliance can be improved by operating in HLSS mode. In our example, the first part of the undulator is tuned to the fundamental wavelength of 3 nm and the third harmonic is used to seed the second part of the undulator tuned to the fundamental wavelength of 1 nm. The coherence time is improved by 70% compared with the SASE mode.

Short-period undulators can be applied to upgrade the existing FEL facilities towards shorter wavelengths while keeping the undulator length unchanged. With superconducting undulator technology, the total active undulator length required to bring the FEL lasing to saturation can be as short as 12 m at a lasing wavelength of $\lambda = 1$ nm. At $\lambda = 5$ nm, the required undulator length is around 8 m. For comparison, at the FLASH facility (Honkavaara, 2018) in Germany, the FEL saturation at the same wavelength of 5 nm is reached within an active undulator length of around 20 m. Therefore, our study underpins the potential of making new X-ray FELs more compact than the existing ones, by taking advantage of the advancements in magnetic undulator technologies. Such high-brilliance X-ray FELs would offer new opportunities to all manners of user experiments and would increase the scientific output.

APPENDIX *A*
1D FEL theory

The 1D theory characterizes the FEL performance by the dimensionless *Pierce parameter*, which is defined as (Bonifacio *et al.*, 1984)

$$\rho = \frac{1}{2\gamma}\left(\frac{I_0}{I_A}\right)^{1/3}\left(\frac{\lambda_u K f_B}{2\pi\sigma_x}\right)^{2/3}. \tag{7}$$

Here, σ_x is the r.m.s. transverse radius of the electron beam, and I_0 is the peak current. Moreover, $I_A = 4\pi\epsilon_0 m_e c^3/e$ is the Alfvén current, where ϵ_0 is the vacuum permittivity constant. For a planar undulator, the coupling factor

$$f_B = J_0\left(\frac{K^2}{4+2K^2}\right) - J_1\left(\frac{K^2}{4+2K^2}\right) \tag{8}$$

comprises two Bessel functions. For a helical undulator, $f_B = 1$. In terms of the Pierce parameter ρ, the *gain length* can be written as (Huang & Kim, 2007)

$$L_{g,1D} = \frac{\lambda_u}{4\sqrt{2}\pi\rho}. \tag{9}$$

Meanwhile, the *saturation length* can be estimated as (Huang & Kim, 2007)

$$L_{sat,1D} \simeq \frac{\lambda_u}{\rho}, \tag{10}$$

and the *saturation power* can be estimated as (Huang & Kim, 2007)

$$P_{sat,1D} \simeq \rho P_{beam}, \tag{11}$$

where $P_{beam} = \gamma m_e c^2 I_0/e$ is the electron beam power. In equation (11), ρ can be interpreted as the *efficiency* of the FEL in converting the electron beam power into radiation power. For X-ray FELs, ρ is typically of the order of 10^{-3}.

APPENDIX *B*
3D FEL theory

B1. Saturation length and saturation power

The 1D FEL theory is an ideal case. It assumes that the electron beam has (i) negligible emittance and (ii) a uniform transverse spatial distribution.

The Ming Xie parametrization (Xie, 2000) accounts for the deviations from the 1D theory, and formulates the gain length in the 3D theory as

$$L_g = \left[1 + \Lambda(\eta_d, \eta_\epsilon, \eta_\gamma)\right] L_{g,1D}, \tag{12}$$

with the correction factor

$$\begin{aligned}\Lambda(\eta_d, \eta_\epsilon, \eta_\gamma) = {} & a_1\eta_d^{a_2} + a_3\eta_\epsilon^{a_4} + a_5\eta_\gamma^{a_6} + a_7\eta_\epsilon^{a_8}\eta_\gamma^{a_9} + a_{10}\eta_d^{a_{11}}\eta_\gamma^{a_{12}} \\ & + a_{13}\eta_d^{a_{14}}\eta_\epsilon^{a_{15}} + a_{16}\eta_d^{a_{17}}\eta_\epsilon^{a_{18}}\eta_\gamma^{a_{19}}.\end{aligned} \tag{13}$$

The correction factor is a function of three variables:

$$\eta_d = \left(\frac{\lambda}{4\pi\sigma_x^2}\right) L_{g,1D} \tag{14}$$

measures the gain reduction due to diffraction,

$$\eta_\epsilon = \left(\frac{4\pi\epsilon}{\lambda}\right)\left(\frac{L_{g,1D}}{\beta}\right) \tag{15}$$

measures the gain reduction due to the emittance ϵ, and

$$\eta_\gamma = \left(\frac{\sigma_\gamma}{\gamma}\right)\left(\frac{L_{g,1D}}{\lambda_u}\right) \tag{16}$$

Table 4
Coefficients for the Ming Xie parametrization.

$a_1 = 0.45$	$a_2 = 0.57$	$a_3 = 0.55$	$a_4 = 1.6$
$a_5 = 3$	$a_6 = 2$	$a_7 = 0.35$	$a_8 = 2.9$
$a_9 = 2.4$	$a_{10} = 51$	$a_{11} = 0.95$	$a_{12} = 3$
$a_{13} = 5.4$	$a_{14} = 0.7$	$a_{15} = 1.9$	$a_{16} = 1140$
$a_{17} = 2.2$	$a_{18} = 2.9$	$a_{19} = 3.2$	Source: (Xie, 2000)

measures the gain reduction due to the r.m.s. energy spread $\sigma_\gamma m_e c^2$.

Recall that the r.m.s. transverse radius of the electron beam is given by $\sigma_x = \left(\bar{\beta}\epsilon\right)^{1/2}$, where $\bar{\beta}$ is the average of the beta function. Recall also that the emittance ϵ can be written in terms of the normalized emittance ϵ_n as $\epsilon = \epsilon_n/\gamma$.

The coefficients a_j ($j = 1, 2, \ldots, 19$) are determined by fitting the numerical solution of the coupled Maxwell Vlasov equations, and their values are listed in Table 4.

By extension, the saturation power and saturation length in 3D theory can be obtained from the following formulae (Xie, 2000):

$$P_{\rm sat} \simeq 1.6\rho\left(\frac{L_{\rm g,1D}}{L_{\rm g}}\right)^2 P_{\rm beam}, \tag{17}$$

$$L_{\rm sat} = L_{\rm g}\ln\left(\frac{P_{\rm sat}}{\alpha P_0}\right). \tag{18}$$

Here, $\alpha = 1/9$ is the scaling factor and P_0 is the initial radiation power. For a SASE FEL we have the effective shot noise power: $P_0 \simeq \rho^2\gamma m_e c^3/\lambda$.

B2. Coherence properties

The coherence properties of a SASE FEL can be analysed in the approach of Saldin *et al.* (2010). The *coherence time* at saturation can be estimated as

$$\tau_{\rm c} \simeq \frac{1}{\bar{\rho}\omega}\left(\frac{\pi\ln N_{\rm c}}{18}\right)^{1/2}, \tag{19}$$

where $N_{\rm c} = I/(e\bar{\rho}\omega)$ is the number of cooperating electrons, $\omega = 2\pi c/\lambda$ is the angular frequency of the radiation, $\bar{\rho} = \rho D^{1/3}$ is the equivalent of the Pierce parameter in 3D theory, $D = 2\Gamma\sigma_x^2\omega/c$ is the diffraction parameter and

$$\Gamma = \left(\frac{I_0}{I_{\rm A}}\frac{8\pi^2K^2f_{\rm B}^2}{\lambda\lambda_{\rm u}\gamma^3}\right)^{1/2} \tag{20}$$

is the gain parameter. The *degree of transverse coherence* at saturation is given by the fitting formula

$$\zeta \simeq \frac{1.1\hat{\epsilon}^{1/4}}{1 + 0.15\hat{\epsilon}^{9/4}}, \tag{21}$$

where $\hat{\epsilon} = 2\pi\epsilon/\lambda$ is the scaled emittance. Note that the fit in equation (21) is done for $N_{\rm c} = 4 \times 10^6$.

From the saturation power (17), we may compute the photon flux:

$$\dot{N}_{\rm ph} = \frac{{\rm d}N_{\rm ph}}{{\rm d}t} = \frac{P_{\rm sat}}{hc/\lambda}. \tag{22}$$

From here, we may compute the *degeneracy parameter*,

$$\delta = \dot{N}_{\rm ph}\tau_c\zeta, \tag{23}$$

and hence the *peak brilliance*,

$$B = \frac{4\sqrt{2}c\delta}{\lambda^3}, \tag{24}$$

at saturation. It is customary to express the peak brilliance in the unit of photons s^{-1} mm^{-2} $mrad^{-2}$ (0.1% bandwidth)$^{-1}$. Note that equation (24) assumes a Gaussian-like radiation spectrum, whose r.m.s. bandwidth is given by $\sigma_\omega = (\pi)^{1/2}/\tau_{\rm c}$.

APPENDIX C
Harmonic lasing

Consider two operation modes for the same output wavelength: SASE and HLSS. The latter enables an enhancement in coherence time (and hence peak brilliance) over the former. The enhancement factor R is given by equation (6), in which the quantity $L_{{\rm sat},h}$, the saturation length of the harmonic lasing, can be estimated as (Schneidmiller & Yurkov, 2012)

$$L_{{\rm sat},h} \simeq 0.6L_{{\rm g},h}\ln\left(hN_{\lambda h}\frac{L_{{\rm g},h}}{\lambda_{\rm u}}\right). \tag{25}$$

Here $N_{\lambda h}$ is the number of electrons per wavelength for harmonic number h and $L_{{\rm g},h}$ is the gain length of the harmonic.

The reduced gain length for the harmonic generation compared with the fundamental of the same wavelength can be clearly demonstrated for variable-gap undulators with a fixed undulator period. In this case, the ratio between the gain length $L_{\rm g,1}$ of the fundamental and the gain length $L_{{\rm g},h}$ of the hth harmonic is given by (Schneidmiller & Yurkov, 2012)

$$\frac{L_{\rm g,1}}{L_{{\rm g},h}} = \frac{h^{1/2}K_hA_{{\rm JJ}h}(K_h)}{KA_{\rm JJ1}(K)}, \tag{26}$$

where K_h and K are the undulator parameters of the first section (tuned to the harmonic) and second section (tuned to the fundamental), respectively. Also,

$$A_{{\rm JJ}h}(K_h) = J_{(h-1)/2}\left(\frac{hK_h^2}{2(1+K_h^2)}\right) - J_{(h+1)/2}\left(\frac{hK_h^2}{2(1+K_h^2)}\right) \tag{27}$$

is the coupling factor for the hth harmonic (Schneidmiller & Yurkov, 2012), where J_n denotes a Bessel function. The ratio $L_{\rm g,1}/L_{\rm g,3} \simeq 1.4$ for high K_3 values and increases rapidly for decreasing K_3 values approaching $\sqrt{2}$, where lasing at the fundamental becomes impossible. Generally $L_{\rm sat} \simeq 10L_{\rm g}$.

Acknowledgements

The authors thank Jim Clarke, Neil Thompson (Daresbury Laboratory, United Kingdom), Marie-Emmanuelle Couprie (SOLEIL, France) and Sverker Werin (MAX IV, Sweden) for the helpful discussions.

Funding information

The simulations were performed on resources provided by the Swedish National Infrastructure for Computing (SNIC) through the Uppsala Multidisciplinary Centre for Advanced Computational Science (UPPMAX) under project SNIC 2017/7–338. The authors acknowledge the following sources of financial support: the European Union's Horizon 2020 Research and Innovation Programme (grant No. 777431); Swedish Research Council (Vetenskapsrådet) (grant No. 2016–04593 awarded to VG); Royal Swedish Academy of Sciences (KVA) (grant No. PH2018-0037 awarded to AM); Stockholm-Uppsala Centre for Free-Electron Laser Research (SUFEL).

References

Altarelli, M. *et al.* (2007). *The European X-ray Free-Electron Laser.* Technical Design Report. DESY, Hamburg, Germany.

Bahrdt, J., Frentrup, W., Grimmer, S., Kuhn, C., Rethfeldt, C., Scheer, M. & Schulz, B. (2018). *Proceedings of the 9th International Particle Accelerator Conference (IPAC2018)*, 29 April–4 May 2018, Vancouver, BC, Canada, pp. 4114–4116. THPMF031.

Bahrdt, J. & Gluskin, E. (2018). *Nucl. Instrum. Methods Phys. Res. A*, **907**, 149–168.

Bencivenga, F., Capotondi, F., Principi, E., Kiskinova, M. & Masciovecchio, C. (2015). *Adv. Phys.* **63**, 327–404.

Bonifacio, R., Pellegrini, C. & Narducci, L. (1984). *Opt. Commun.* **50**, 373–378.

Cahn, R. S., Ingold, C. & Prelog, V. (1966). *Angew. Chem. Int. Ed. Engl.* **5**, 385–415.

Capotondi, F., Pedersoli, E., Bencivenga, F., Manfredda, M., Mahne, N., Raimondi, L., Svetina, C., Zangrando, M., Demidovich, A., Nikolov, I., Danailov, M., Masciovecchio, C. & Kiskinova, M. (2015). *J. Synchrotron Rad.* **22**, 544–552.

Capotondi, F., Pedersoli, E., Mahne, N., Menk, R. H., Passos, G., Raimondi, L., Svetina, C., Sandrin, G., Zangrando, M., Kiskinova, M., Bajt, S., Barthelmess, M., Fleckenstein, H., Chapman, H. N., Schulz, J., Bach, J., Frömter, R., Schleitzer, S., Müller, L., Gutt, C. & Grübel, G. (2013). *Rev. Sci. Instrum.* **84**, 051301.

Chapman, H. N., Barty, A., Bogan, M. J., Boutet, S., Frank, M., Hau-Riege, S. P., Marchesini, S., Woods, B. W., Bajt, S., Benner, W. H., London, R. A., Plönjes, E., Kuhlmann, M., Treusch, R., Düsterer, S., Tschentscher, T., Schneider, J. R., Spiller, E., Möller, T., Bostedt, C., Hoener, M., Shapiro, D. A., Hodgson, K. O., van der Spoel, D., Burmeister, F., Bergh, M., Caleman, C., Huldt, G., Seibert, M. M., Maia, F. R. N. C., Lee, R. W., Szöke, A., Timneanu, N. & Hajdu, J. (2006). *Nat. Phys.* **2**, 839–843.

Compact Light Collaboration (2018–2020). *Compact Light Project*, http://www.compactlight.eu/.

Craievich, P. (2010). PHD thesis, Technische Universiteit Eindhoven, Germany (http://repository.tue.nl/676789).

Dejus, R., Jaski, M. & Kim, S. H. (2009). *On-axis brilliance and power of in-vacuum undulators for the Advanced Photon Source.* Technical Report ANL/APS/LS-314. Argonne National Laboratory, Argonee, IL, USA.

Galayda, J. (2018). *Proceedings of the 9th International Particle Accelerator Conference (IPAC2018)*, 29 April–4 May 2018, Vancouver, BC, Canada, pp. 18–23. MOYGB2.

Halbach, K. (1983). *J. Phys. Colloq.* **44**, C1-211–C1216.

Honkavaara, K. (2018). *Proceedings of the 38th International Free-Electron Laser Conference (FEL2017)*, 20–25 August 2017, Santa Fe, NM, USA, pp. 14–18. MOD02.

Huang, J.-C., Kitamura, H., Yang, C.-K., Chang, C.-H., Chang, C.-H. & Hwang, C.-S. (2017). *Phys. Rev. Accel. Beams*, **20**, 064801.

Huang, Z. (2015). *Proceedings of the 37th International Free Electron Laser Conference (FEL2015)*, 23–28 August 2015, Daejeon, Korea, pp. 7–9. MOB02.

Huang, Z. & Kim, K.-J. (2007). *Phys. Rev. ST Accel. Beams*, **10**, 034801.

Kim, S. (2005). *Nucl. Instrum. Methods Phys. Res. A*, **546**, 604–619.

Ko, I., Kang, H.-S., Heo, H., Kim, C., Kim, G., Min, C.-K., Yang, H., Baek, S., Choi, H.-J., Mun, G., Park, B., Suh, Y., Shin, D., Hu, J., Hong, J., Jung, S., Kim, S.-H., Kim, K., Na, D., Park, Y., Park, Y., Jung, Y., Jeong, S., Lee, S., Lee, S., Lee, S., Oh, B., Suh, H., Han, J., Kim, M., Jung, N., Kim, Y., Lee, M., Lee, B., Sung, C., Mok, I., Yang, J., Parc, Y., Lee, W., Lee, C., Shin, H., Kim, Y., Kim, Y., Lee, J., Park, S., Kim, J., Park, J., Eom, I., Rah, S., Kim, S., Nam, K. H., Park, J., Park, J., Kim, S., Kwon, S., An, R., Park, S., Kim, K., Hyun, H., Kim, S., Kim, S., Yu, C., Kim, B., Kang, T., Kim, K., Kim, S., Lee, H.-S., Lee, H., Park, K., Koo, T., Kim, D. & Lee, K. (2017). *Appl. Sci.* **7**, 479.

Kondratenko, A. M. & Saldin, E. L. (1980). *Part. Accel.* **10**, 207–216.

Lutman, A. A., MacArthur, J. P., Ilchen, M., Lindahl, A. O., Buck, J., Coffee, R. N., Dakovski, G. L., Dammann, L., Ding, Y., Dürr, H. A., Glaser, L., Grünert, J., Hartmann, G., Hartmann, N., Higley, D., Hirsch, K., Levashov, Y. I., Marinelli, A., Maxwell, T., Mitra, A., Moeller, S., Osipov, T., Peters, F., Planas, M., Shevchuk, I., Schlotter, W. F., Scholz, F., Seltmann, J., Viefhaus, J., Walter, P., Wolf, Z. R., Huang, Z. & Nuhn, H.-D. (2016). *Nat. Photon.* **10**, 468–472.

Mancuso, A. P., Gorniak, T., Staier, F., Yefanov, O. M., Barth, R., Christophis, C., Reime, B., Gulden, J., Singer, A., Pettit, M. E., Nisius, T., Wilhein, T., Gutt, C., Grübel, G., Guerassimova, N., Treusch, R., Feldhaus, J., Eisebitt, S., Weckert, E., Grunze, M., Rosenhahn, A. & Vartanyants, I. A. (2010). *New J. Phys.* **12**, 035003.

Moog, E. R., Dejus, R. J. & Sasaki, S. (2017). *Comparison of Achievable Magnetic Fields with Superconducting and Cryogenic Permanent Magnet Undulators – A Comprehensive Study of Computed and Measured Values.* Technical Report ANL/APS/LS-348 137001. Argonne National Laboratory, Argonne, IL, USA.

Mukamel, S., Healion, D., Zhang, Y. & Biggs, J. D. (2013). *Annu. Rev. Phys. Chem.* **64**, 101–127.

Neutze, R., Brändén, G. & Schertler, G. F. (2015). *Curr. Opin. Struct. Biol.* **33**, 115–125.

Reiche, S. (1999). *Nucl. Instrum. Methods Phys. Res. A*, **429**, 243–248.

Saldin, E. L., Schneidmiller, E. A. & Yurkov, M. V. (2010). *New J. Phys.* **12**, 035010.

Schneidmiller, E. A., Faatz, B., Kuhlmann, M., Rönsch-Schulenburg, J., Schreiber, S., Tischer, M. & Yurkov, M. V. (2017). *Phys. Rev. Accel. Beams*, **20**, 020705.

Schneidmiller, E. A. & Yurkov, M. V. (2012). *Phys. Rev. ST Accel. Beams*, **15**, 080702.

Schneidmiller, E. A. & Yurkov, M. V. (2013). *Phys. Rev. ST Accel. Beams*, **16**, 110702.

Seddon, E. A., Clarke, J. A., Dunning, D. J., Masciovecchio, C., Milne, C. J., Parmigiani, F., Rugg, D., Spence, J. C. H., Thompson, N. R., Ueda, K., Vinko, S. M., Wark, J. S. & Wurth, W. (2017). *Rep. Prog. Phys.* **80**, 115901.

Smolentsev, G. & Sundström, V. (2015). *Coord. Chem. Rev.* **304–305**, 117–132.

Ullrich, J., Rudenko, A. & Moshammer, R. (2012). *Annu. Rev. Phys. Chem.* **63**, 635–660.

Weckert, E. (2015). *IUCrJ*, **2**, 230–245.

Werin, S., Andersen, J., Bonetti, S., Curbis, F., Goryashko, V., Isaksson, L., Johnsson, P., Kotur, M., Larsson, M., Lindau, F., Mansten, E., Nilsson, A., Olsson, D., Salén, P., Tarawneh, H., Tavares, P., Thorin, S. & Tjernberg, O. (2017). *Proceedings of the 8th International Particle Accelerator Conference (IPAC2017)*, 14–19 May 2017, Copenhagen, Denmark, pp. 2760–2762.

Xie, M. (2000). *Nucl. Instrum. Methods Phys. Res. A*, **445**, 59–66.